

Experimental Limit on the Cosmic Diffuse Ultra-high Energy Neutrino Flux

P. W. Gorham,^{1,2} C. L. Hebert,¹ K. M. Liewer,² C. J. Naudet,² D. Saltzberg,³ and D. Williams³

¹*Dept. of Physics & Astronomy, Univ. of Hawaii at Manoa, 2505 Correa Rd. Honolulu, HI, 96822*

²*Jet Propulsion Laboratory, Calif. Inst. of Technology, Pasadena, CA, 91109*

³*Dept. of Physics & Astronomy, Univ. of Calif. Los Angeles, Los Angeles, CA*

We report results from 120 hours of livetime with the Goldstone Lunar Ultra-high energy neutrino Experiment (GLUE). The experiment searches for ≤ 10 ns microwave pulses from the lunar regolith, appearing in coincidence at two large radio telescopes separated by 22 km and linked by optical fiber. Such pulses would arise from subsurface electromagnetic cascades induced by interactions of ≥ 100 EeV neutrinos in the lunar regolith. Triggering on a timing coincidence between the two telescopes significantly reduces the terrestrial interference background, allowing operation at the thermal noise level. No candidates are yet seen. We report on limits implied by this non-detection, based on Monte Carlo estimates of the efficiency.

In 1962, G. Askaryan predicted [1] that electromagnetic cascades in dense media should produce strong coherent pulses of microwave Cherenkov radiation. Recent confirmation of this hypothesis at accelerators [2, 3] strengthens the motivation to use this effect to search for cascades induced by predicted diffuse backgrounds of high energy neutrinos, which are associated with the presence of $\geq 10^{20}$ eV cosmic rays in many models.

Neutrinos with energies above 100 EeV (1 EeV = 10^{18} eV) can produce cascades in the upper 10 m of the lunar regolith resulting in pulses that are detectable at Earth by large radio telescopes. [4, 5] One prior experiment has been reported, using the Parkes 64 m telescope [6] with 10 hours of livetime. In the decimeter microwave band, the signal should appear as highly linearly-polarized, band-limited electromagnetic impulses [7, 8, 9, 10]. However, since there are many anthropogenic sources of impulsive radio-frequency interference (RFI), the primary problem in detecting neutrinos is to reject such interference. Since 1999 we have been conducting a series of experiments in search of such pulses, using the JPL/NASA Deep Space Network antennas at Goldstone, California [11]. We have essentially eliminated RFI background by employing the 70 m (DSS14) and 34 m (DSS13) antennas in coincidence.

Although the total livetime accumulated in our experiment is a relatively small fraction of what is possible with a dedicated system, the volume of material to which we are sensitive is enormous, exceeding 100,000 km³ at the highest energies. The resulting sensitivity is enough to begin constraining some models for diffuse neutrino fluxes at energies above 10^{20} eV. We report here on results from 120 hours of livetime.

The lunar regolith is an aggregate layer of fine particles and small rocks, thought to be the accumulated ejecta of meteor impacts with the lunar surface. It consists mostly of silicates and related minerals, with meteoritic iron and titanium compounds at an average level of several per cent, and traces of meteoritic carbon. It has a typical depth of 10 to 20 m in the maria and valleys, but may be hundreds of meters deep in portions of the highlands [12]. It has a mean dielectric constant of $\epsilon \simeq 3$ and a density of

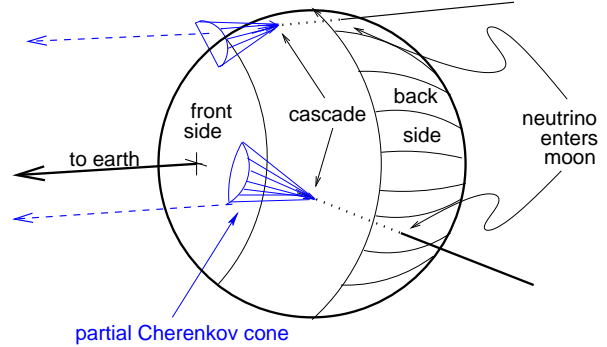


FIG. 1: Schematic of the geometry for lunar neutrino cascade event detection.

$\rho \simeq 1.7$ g cm⁻³, both increasing slowly with depth. Measured values for the loss tangent vary widely depending on iron and titanium content, but a mean value at high frequencies is $\tan \delta \simeq 0.003$, implying a field attenuation length at 2 GHz of $(\alpha)^{-1} = 9$ m [13].

In Fig. 1 we illustrate the signal emission geometry. At 100 EeV the interaction length of a neutrino is about 60 km [14]. Upon interaction, a cascade ~ 10 m long forms as the secondary particles multiply, and Compton scattering, positron annihilation, and other processes lead to a $\sim 20\%$ negative charge excess. This cascade radiates a cone of coherent Cherenkov emission at an angle of 56° , with an angular spread of $\sim 1^\circ$ at 2 GHz. The radiation propagates in the form of a sub-ns pulse through the regolith to the surface where it is refracted forward upon transmission. Scattering from surface irregularities and demagnification from the interface refraction gradient fills in the Cherenkov cone, and results in a larger effective area of the lunar surface over which events can be detected.

The antennas employed in our search are the shaped-Cassegrainian 70 m antenna DSS14, and the 34 m beam-

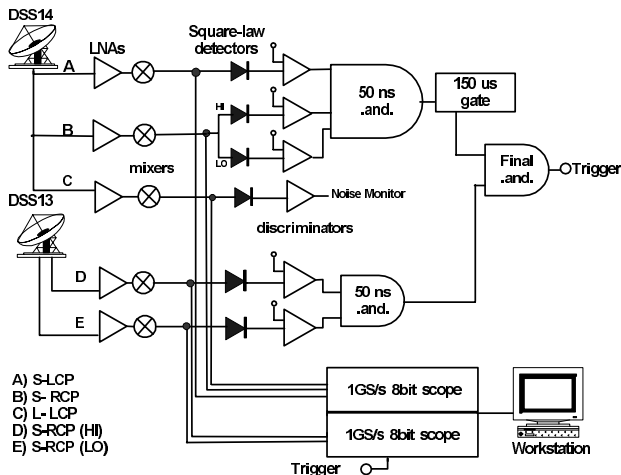


FIG. 2: GLUE trigger & data recording system.

waveguide antenna DSS13, both part of the NASA Goldstone Deep Space Network Tracking Station and separated by 22 km. The S-band (2.2 GHz) right-circular-polarization (RCP) signal from DSS13 is filtered to 150 MHz bandwidth and down-converted to an intermediate frequency (IF) near 300 MHz. The band is subdivided into high and low frequency halves with no overlap. The DSS14 dual polarization S-band signals are down-converted to the same 300 MHz IF, and bandwidths of 150 MHz (RCP) and 40 MHz (LCP) are used. In recent operation, the 150 MHz IF has been split into two 75 MHz bands to improve the trigger performance. At DSS14, an L-band (1.8 GHz) feed which is off-pointed by $\sim 0.5^\circ$ produces a 40 MHz bandwidth monitor of terrestrial interference signals that is recorded along with the other signals.

Fig. 2 shows the layout of the trigger. The four (or five if the DSS14 split RCP is used) triggering signals from the two antennas are converted to unipolar pulses using tunnel-diode square-law detectors with a ~ 10 ns integration time. These pulses are discriminated to a roughly constant singles rate. In the 4 channel system, the rates are 0.5–1 kHz for DSS14, and 30 kHz for DSS13 to compensate for its reduced aperture size. In the more recent 5-channel system, the singles rates are increased to approximately 30 kHz for the RCP channels, and 45 kHz for the DSS14 LCP channel. A local coincidence within 50 ns is formed among each antenna’s channels. The DSS14 coincidence between both circular polarizations ensures that the signals are highly linearly polarized, and the DSS13 and DSS14 split-channel coincidence ensures that the triggered signal is broadband.

A global trigger is formed between the local coincidences of the two antennas within a $150 \mu\text{s}$ window. A fixed delay compensates for the $136 \mu\text{s}$ fiber delay between the two antennas. This large time window encompasses the possible geometric delay range for the Moon throughout the year. Although use of a smaller window

is possible, a tighter coincidence will be required offline and the out-of-time events provide a large background sample. Upon the global coincidence, two sampling oscilloscopes are triggered, and a $250 \mu\text{s}$ record, sampled at 1 GSa/s, is stored. The average trigger rate, due primarily to random coincidences of thermal noise fluctuations, is 3×10^{-3} Hz. Terrestrial interference triggers are a few percent of the total, but can occasionally increase in number when a large burst of interference occurs at either antenna. To avoid recording large bursts of terrestrial noise, a 6 s holdoff is employed after each trigger. Thus we maintain $\geq 95\%$ livetime during a run.

The precise geometry of the experiment is a crucial discriminator for events from the Moon. Let \vec{B} be the baseline vector between the two antennas. The relative delay between the two antennas is $\tau = c^{-1}|\vec{B}|\cos\theta$ where θ is the apparent angle of the Moon with respect to the baseline vector. For our 22 km baseline, we have a maximum delay difference of $\tau_{max} = \pm 73 \mu\text{s}$. Detectable events can occur anywhere on the Moon’s surface within the antenna beam. This produces a possible spread of 630 ns in the differential delay of the received pulses at the two antennas.

The 2.2 GHz antenna beamwidths between the first Airy nulls are nominally 0.27° for the 70 m, and 0.56° for the 34 m. We took data in three configurations: pointing at the limb, the center, and halfway between. The measured source temperatures varied from 70K at the limb, to 160K at the Moon center, with system temperatures of 30-40K.

Timing and amplitude calibration are accomplished in several steps. We internally calibrate the back-end trigger system using a synthesized IF pulse signal, giving precision of order 1 ns. We then use a 2.2 GHz monocyple pulse transmitter aimed at the antennas to calibrate the cross-channel delays of each antenna to a precision of 2 ns. The cross-polarization timing at DSS 14 is also checked with a second method which utilizes the fact that the thermal radiation from the limb of the Moon is significantly linearly polarized (from differential Fresnel effects [15, 16]), and this introduces an easily detectable LCP-to-RCP correlation.

Dual antenna timing calibration is accomplished by cross-correlating a $250 \mu\text{s}$ thermal noise sample of a bright quasar, typically 3C273, recorded from both antennas at the same time and in the same polarization, using the identical data acquisition system used for the pulse detection. This procedure establishes the delay offset between the two antennas, which is of order $136 \mu\text{s}$. Repeating the procedure with approximately ten different quasars shows a reproducibility better than 10 ns.

Amplitude calibration is accomplished by the standard methods of radio astronomy, by referencing to a thermal noise source at a known temperature. The measured system temperature during a run fixes the value of the noise level and therefore the energy threshold. We also check linearity for pulsed transient response using monocyple generators and this ensures that the entire system has

the dynamic range required to see large pulses.

Figure 3 shows a typical event which triggered the system. The top two panes contain the DSS14 LCP and RCP signals, and a narrow pulse is present in both polarizations, indicating a broadband spectral content, and a high degree of linear polarization. The pulse power is normalized to the local mean power over a 250 μs window. In the third and fourth panes, the two channels from DSS13 are shown. In the fifth pane from the top the L-band offset feed signal from DSS 14 is shown, and no RFI noise is present. The measured delay relative to the expected Moon time is shown as $-1.1 \mu\text{s}$ in this case, slightly larger than what can be nominally allowed. Systematic timing offsets from channel to channel are typically well under 10 ns in these data.

Two largely independent analyses look for pulses corresponding to an electric field 6σ above thermal noise in all channels. Both analyses remove terrestrial RFI with either a visual or algorithmic method. Each enforces ~ 20 ns local coincidence timing at each antenna. In both cases, the precise values of the cuts were determined and fixed before looking at more than half of the data analyzed. To date we have seen no candidates in 120 hours of livetime. The signal efficiency of the RFI and timing cuts is estimated to be $> 98\%$. To estimate background levels, we also search of order 100 different delay values that are inconsistent with the Moon's sky position, and we have also found no candidates in this search. Hence we observe no events with a background of ≤ 0.01 events.

Because much of the theoretical work in describing such pulses has been done in terms of field strength rather than power, we analyze our sensitivity in these terms. Such analysis is also compatible with the receiving system, which records antenna voltages proportional to the incident electric field, and leads to a more linear analysis. It also yields signal-to-noise ratio estimates which are consistent with Gaussian statistics, since thermal noise voltages are described by a Gaussian random process.

The expected field strength per unit bandwidth from a cascade of total energy W_T in regolith material can be expressed as [7, 9]:

$$E_0 \text{ (V m}^{-1} \text{ MHz}^{-1} \text{)} = \frac{1.45 \times 10^{-7}}{R} \left(\frac{W_T}{1 \text{ TeV}} \right) \times \frac{\nu}{\nu_0} \left(\frac{1}{1 + (\nu/\nu_0)^{1.44}} \right), \quad (1)$$

where R is the distance to the source in meters, ν is the radio frequency, and the decoherence frequency is $\nu_0 \simeq 2500$ MHz for the regolith (ν_0 scales mainly by radiation length). For typical parameters in our experiment, a 10^{20} eV cascade will result in a peak field strength at Earth of $E \simeq 1.3 \mu\text{V m}^{-1}$ for a 70 MHz bandwidth. Equation 1 has now been verified to within a factor of 2 through accelerator tests [2, 3] using silica sand targets and γ -ray-induced cascades with composite $W_T \sim 10^{19}$ eV.

Based on the effective antenna aperture ηA and the fact that the background events are due to fluctuations in

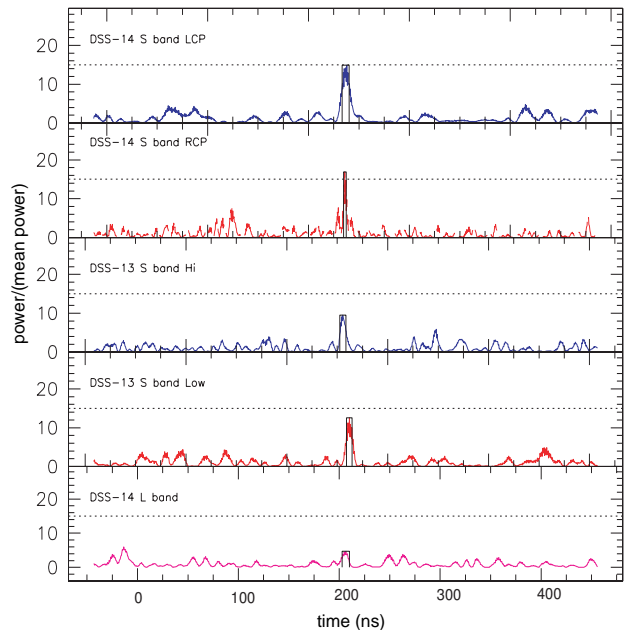


FIG. 3: An example of a triggered event. The displayed signals are, from top to bottom: the LCP intensity at DSS14; the RCP intensity; the high-band intensity at DSS13; the low-band intensity at DSS13; the L-band off-axis interference monitor (no interference present).

the black-body power of the Moon, we estimate that the minimum detectable field strength for a linearly polarized pulse

$$E_{min} = N_\sigma \sqrt{\frac{2kT_{sys}Z_0}{\eta A \Delta\nu \sqrt{\epsilon}}}, \quad (2)$$

where $Z_0 = 377\Omega$, and N_σ the number of standard deviations required per channel relative to thermal fluctuations. Combining this with equation 1 above, we estimate the threshold energy for pulse detection. For the lunar observations on the limb, which make up about 85% of the data reported here, $T_{sys} \simeq 110$ K (including the source contribution), $\nu = 2.2$ GHz, and the average $\Delta\nu \simeq 70$ MHz. For the 70 m antenna, with efficiency $\eta \simeq 0.8$, the minimum detectable field strength at $N_\sigma = 6$ is $E_{min} \simeq 0.8 \mu\text{V m}^{-1}$. The estimated cascade threshold energy for these parameters is $W_{thr} = 6 \times 10^{19}$ eV. Since the mean inelasticity is $\langle y \rangle = 0.2$ for deep inelastic scattering (the most probable cascade channel) at these energies, typical neutrino events at threshold will have an energy of $\sim 3 \times 10^{20}$ eV.

To estimate the effective volume and acceptance solid angle as a function of incoming neutrino energy, we have used two independent Monte Carlo simulations to generate events at discrete neutrino energies, including the current best estimates of both charged and neutral current cross sections [14], and the Bjorken- y distribution. The neutrino species are assumed to be fully mixed upon arrival. Both electron and muon neutrino interactions

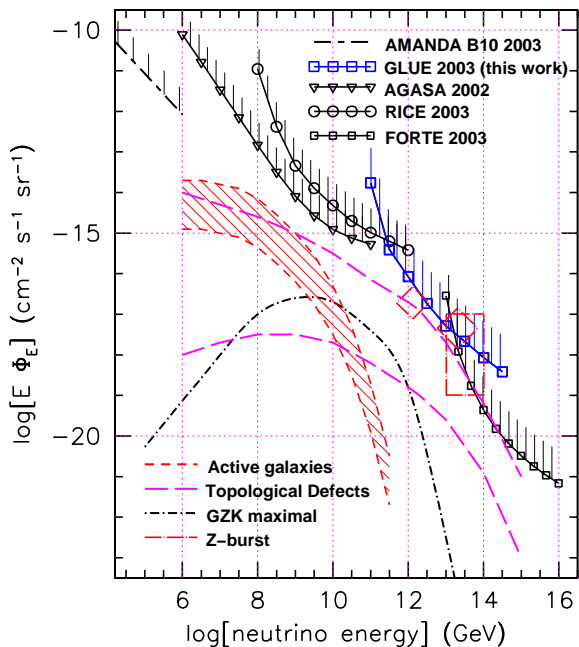


FIG. 4: Model neutrino fluxes, and limits from the present work and several other current experiments.

were included, and Landau-Pomeranchuk-Migdal effects in the shower formation were estimated [8]. At each neutrino energy, a distribution of cascade angles and depths with respect to the local surface was obtained, and a refraction propagation of the predicted Cherenkov angular distribution was made through the regolith surface, including absorption and reflection losses and a first order roughness model. Thermal noise fluctuations were included in the detection process.

Our simulations (see Ref. [17] for details and illustrations) find that, although the specific flux density of the events are lowered somewhat by refraction and scattering, the effective volume and acceptance solid angle are significantly increased. The neutrino acceptance solid angle, in particular, is about a factor of 20 larger than the apparent solid angle of the Moon itself. We note that UHE cosmic rays will at some level produce a background for lunar neutrino detection. However, there are several processes that suppress cosmic ray radio emission with respect to that of neutrinos, including total internal reflection, and formation zone effects [17].

Figure 4 plots the predicted fluxes of ultra-high energy (UHE) neutrinos from a number of models including AGN production [18, 19] a maximal flux from UHE cosmic-ray interactions [20], two topological defect models [21, 22], and the Z-burst scenario [23, 24]. Several current limits in this energy regime are plotted, from recent analysis of AGASA data [25], the RICE experiment [26], and new limits from the FORTE satellite [27]. Our 90% confidence level, differential model-independent limit for 120 hours of livetime is shown plotted with large squares [28], based on the observation of no events above an equivalent 6σ level amplitude (referenced to the 70 m antenna) consistent with the direction of the Moon. Combined GLUE and FORTE results indicate that the highest topological defect model [21], which should produce $\sim 10-30$ events in each detector, now appears to be largely excluded. We also exclude a significant portion of the Z-burst parameter space.

All of the limit curves in Fig. 4 (with the exception of the AMANDA limit for an $E_{\nu\mu}^{-2}$ power law spectrum) correspond to the inverse of the energy-dependent exposure = (neutrino aperture \times time) [29] for each detector noted, scaled by the appropriate Poisson upper-limit factor (2.3 for 90% CL). For a typical power-law flux model in Fig. 4, integration over energy would produce $\sim 6-10$ events per decade of energy over which the model equals the curve. Integral limits would thus rule out power-law neutrino models a factor of 3-5 below the plotted differential model-independent curves. Z-burst models require a minimum intensity of neutrinos at the Z0 resonance energy to the explain UHE cosmic rays. For such monoenergetic spectra, the differential limits quoted here are limits on their monenergetic flux. Since the neutrino spectra in Z-burst models are almost certainly much wider than the minimum interval required, the limits are especially conservative.

We thank M. Klein, T. Kuiper, R. Milincic, and the staff at Goldstone for their enthusiastic support of our efforts. We dedicate this work to the memory of George Resch, who passed away in Nov. 2001. Without his encouragement and unflagging support, this work would not have been done. This work was performed in part at the Jet Propulsion Laboratory, California Institute of Technology, under contract with NASA, and supported in part by the Caltech President's Fund, by DOE contract DE-FG03-91ER40662 at UCLA, DOE contract DE-FG03-94ER40833 at the Univ. of Hawaii, the Sloan Foundation, and the National Science Foundation.

[1] G. A. Askaryan, 1962, JETP 14, 441; G. A. Askaryan, 1965, JETP 21, 658.
[2] P. W. Gorham, D. P. Saltzberg, P. Schoessow, *et al.*, Phys. Rev. E. **62**, 8590 (2000).
[3] D. Saltzberg, P. Gorham, D. Walz, *et al.* Phys. Rev. Lett., **86**, 2802 (2001).

[4] I. M. Zheleznykh, 1988, Proc. Neutrino '88, 528.
[5] R. D. Dagkesamanskii, & I. M. Zheleznyk, 1989, JETP 50, 233.
[6] T. H. Hankins, R. D. Ekers & J. D. O'Sullivan, 1996, MNRAS 283, 1027.
[7] E. Zas, F. Halzen,, & T. Stanev, 1992, Phys Rev D 45,

- 362.
- [8] J. Alvarez-Muñiz, & E. Zas, 1997, Phys. Lett. B, 411, 218.
- [9] J. Alvarez-Muñiz, & E. Zas, 2000, in Proc. of RADHEP 2000, AIP#579 (2001).
- [10] S. Razzaque et al., Phys. Rev. D65, 103002 (2002).
- [11] P. Gorham, et al., Proc. 26th ICRC, HE 6.3.15, astro-ph/9906504.
- [12] D. Morrison & T. Own, 1987 *The Planetary System*, (Addison-Wesley: Reading,MA).
- [13] G. R. Olhoeft & D. W. Strangway, 1975, Earth Plan. Sci. Lett. 24, 394.
- [14] R. Gandhi, Nucl.Phys.Proc.Suppl. 91 (2000) 453, hep-ph/0011176.
- [15] N. S. Soboleva, Soviet astronomy - AJ, 6(6), 873, (1963).
- [16] C. E. Heiles and F. D. Drake, Icarus 2, 281 (1963).
- [17] P. Gorham *et al.*, in Proc. of RADHEP 2000, AIP#579 (2001), astro-ph/0102435.
- [18] Mannheim, K., 1996, Astropart. Phys 3, 295.
- [19] F.W. Stecker, M.Salamon, C.Done and P. Sommers, PRL 66, 2697; E69, 2738 (1991); see also Stecker & Salamon, Space Sci. Rev. 75, 341 (1996)
- [20] R. Engel, D. Seckel, & T. Stanev, PRD 64, 093010, (2001).
- [21] S. Yoshida, H. Dai, C. C. H. Jui, & P. Sommers, 1997, ApJ 479, 547.
- [22] Bhattacharjee, P., Hill, C.T., & Schramm, D.N, 1992 PRL 69, 567.
- [23] T. Weiler, 1999, hep-ph/9910316.
- [24] Z. Fodor, S. D. Katz, & A. Ringwald, JHEP 0206:046, (2002); hep-ph/0203198.
- [25] L. A. Anchordoqui et al., Phys. Rev. D 66, 103002 (2002).
- [26] I. Kravchenko et al., for the RICE collaboration, submitted to Astroparticle Physics; astro-ph/0206371, (2003).
- [27] N. Lehtinen, P. Gorham, A. Jacobson, & R. Roussel-Dupré, submitted to PRD; astro-ph/0309656, (2003).
- [28] The values of the 8 plotted points are: -13.8,-15.4,-16.1,-16.7,-17.3,-17.7,-18.1,-18.4.
- [29] Similar to approaches described in ref. [25] and ref. [27], as well as earlier GLUE results [11, 17].